Received: 27 July 2021 | Revised: 19 October 2021 | Accepted: 2 November 2021

DOI: 10.1111/jace.18235

Journal of the American Ceramic Society

RESEARCH ARTICLE

Glass-ceramic composites as insulation material for thermoelectric oxide multilayer generators

Sophie Bresch[1] | **Björn Mieller**[1] | **Paul Mrkwitschka**[1] | **Ralf Moos**[2] | **Torsten Rabe**[1]

[1] Advanced Technical Ceramics, Bundesanstalt für Materialforschung und –prüfung, Unter den Eichen 44-46, Berlin, Deutschland 12203, Germany

[2] Department of Functional Materials, Universität Bayreuth, Bayreuth, Germany

Correspondence
Sophie Bresch, Technische Keramik, Bundesanstalt für Materialforschung und –prüfung, Berlin, Germany.
Email: sophie.bresch@bam.de

Abstract

Thermoelectric generators can be used as energy harvesters for sensor applications. Adapting the ceramic multilayer technology, their production can be highly automated. In such multilayer thermoelectric generators, the electrical insulation material, which separates the thermoelectric legs, is crucial for the performance of the device. The insulation material should be adapted to the thermoelectric regarding its averaged coefficient of thermal expansion α and its sintering temperature while maintaining a high resistivity.

In this study, starting from theoretical calculations, a glass-ceramic composite material adapted for multilayer generators from calcium manganate and calcium cobaltite is developed. The material is optimized towards an α of 11×10^{-6} K^{-1} (20–500°C), a sintering temperature of 900°C, and a high resistivity up to 800°C. Calculated and measured α are in good agreement. The chosen glass-ceramic composite with 45 vol.% quartz has a resistivity of 1×10^{7} Ωcm and an open porosity of <3%. Sintered multilayer samples from tape-cast thermoelectric oxides and screen-printed insulation show only small reaction layers. It can be concluded that glass-ceramic composites are a well-suited material class for insulation layers as their physical properties can be tuned by varying glass composition or dispersion phases.

KEYWORDS

electrical insulators, glass-ceramics, multilayers, thermal expansion

1 | INTRODUCTION

Oxide multilayer generators as first proposed by Hayashi et al.[1] are promising devices for energy harvesting. Thermoelectric materials transform a temperature difference directly into an electric voltage that is described by the Seebeck coefficient. In a thermoelectric generator, materials with positive (p-type) and negative (n-type) Seebeck coefficients are thermally connected in parallel and electrically connected in series. Multilayer generators use ceramic multilayer technology where the thermoelectric materials are tape-cast and the functional layers like metallization and insulation are screen-printed on top of these tapes. The tapes are stacked and co-fired in one step. The fabrication can be highly automated. A schematic drawing is shown in Figure 6A. First prototypes

successfully powered sensor systems.[2,3] Multilayer generators were fabricated from cuprates[1,4] and $SrTiO_3$.[2] At present, promising high-temperature oxidation-resistant thermoelectrics are calcium cobaltite $Ca_3Co_4O_9$ as a p-type material and calcium manganate $CaMnO_3$ as an n-type material.[5,6] For co-fired generators from $CaMnO_3$ and $Ca_3Co_4O_9$, the sintering temperature is limited to 900°C due to the phase stability of $Ca_3Co_4O_9$. The combination of pressure-assisted sintering[7] and sintering additives[8] provides the theoretical possibility of co-sintering these two material systems in one single step.

For successful co-firing and long-term stability of multilayer generators, all layers have to be adapted regarding their sintering temperature, their average coefficient of thermal expansion (α), and their functional properties. For the insulation layer, which separates the p- and n-type thermoelectric oxide, this means a high resistivity, a sintering temperature in the range of the thermoelectric oxides, and an α in between the p- and the n-type material to minimize thermal stresses. In literature, different material classes like ceramics,[2] glasses,[4] and glass-bonded ceramics[1] were used as insulation material for multilayer generators. Ceramics have a defined α and sintering temperature. Doping and powder processing can change these properties to some extent.[9] For example, yttria-stabilized zirconia was used as an insulator for the $SrTiO_3$ and $Ni_{0.9}Mo_{0.1}$ system.[2] In glass systems, properties like thermal expansion can be adapted to a wide range by changing the composition.[10] Computer programs like SciGlass provide the possibility to calculate and predict the influence of composition on properties. A not further described glass system was used by Töpfer et al.[4] for co-sintering doped La_2CuO_4 and doped Nd_2CuO_4. The sintering curve of ceramics with suited thermal expansion coefficients can be tuned by adding 3–20 vol.% glass (glass-bonded ceramics).[11] Hayashi et al. used Mg_2SiO_4 bonded with 5 wt% of a borate glass as an insulation material for multilayer generators from doped La_2CuO_4 and doped Nd_2CuO_4.[1] By varying the glass content, the sintering temperature could be shifted by several 100 degrees.

$CaMnO_3$ and $Ca_3Co_4O_9$ have relatively high averaged α. The α of $CaMnO_3$ is in the order of 11×10^{-6} K^{-1} from 20–700°C.[12,13] $Ca_3Co_4O_9$ has a layered crystal structure and thus shows anisotropic single crystal properties. The α depends on the degree of anisotropy of the polycrystalline material. For materials with a low anisotropy (multiples of random distribution around 3) α is reported in the range of $9–12 \times 10^{-6}$ K^{-1} from 20 to 800°C,[12,14,15] for anisotropic materials (hot-pressed with 30 MPa) α_{ab} is 7×10^{-6} K^{-1} and α_c is 15×10^{-6} K^{-1} from 20 to 800°C.[15] In the case of multilayer generators with tape-cast $Ca_3Co_4O_9$, the α_{ab} is of main interest. To the best of the authors' knowledge, there is no reported successful co-firing of multilayer thermoelectric generators from $Ca_3Co_4O_9$ and $CaMnO_3$. However, spark plasma sintering was used to co-fire powder layers from $Ca_3Co_4O_9$ and $CaMnO_3$ separated by $LaAlO_3$-tapes for insulation by the group around Einarsrud.[16,17] In this respect, this is not a scalable multilayer approach but a fundamental material combination study. The insulation material has an α[17] of 13.4×10^{-6} K^{-1} and a high sintering temperature of 1550°C.[18] The resulting insulation layer is porous and cracks develop from the insulation to the $CaMnO_3$ material.[17] To reduce cracks, insulation materials with lower α like MgO (13×10^{-6} K^{-1}) or $SrZrO_3$ (10×10^{-6} K^{-1}) were theoretically discussed.[17] But due to their high sintering temperatures above 1300°C,[19,20] the systems are unsuitable.

Glass-ceramic composites consist of glass (50–80 vol.%)[11] and usually one dispersion phase. During sintering, one (or more) crystal phases crystallize from the glass. The sintering temperature and the physical properties, such as α, can be specifically influenced by the selection of the glass system and the dispersion phase.[21] At room temperature, glass ceramics are insulators; depending on the residual glass content, the resistivity decreases over temperature. Stresses during cooling by mismatches in the α can be compensated by the residual glass phase up to its transformation temperature. According to Nazare and Ondracek,[22] α of a glass-ceramic composite with a glass phase (subscript "G") and a dispersion phase (subscript "D") can be calculated with volume fraction (V), Young's modulus (E), and Poisson ratio (ν) as follows:

$$\alpha = \alpha_G + \frac{(\alpha_D - \alpha_G) \cdot V_D E_D \cdot (1 - 2\upsilon_G)}{V_G E_G \cdot (1 - 2\upsilon_D) + V_D E_D \cdot (1 - 2\upsilon_G)} \quad (1)$$

In this work, a glass-ceramic composite (BAM397)[21,23] with an α close to steel is adapted for application as an insulating material in multilayer generators composed of $Ca_3Co_4O_9$ and $CaMnO_3$. BAM397 consists of a BaO-B_2O_3-SiO_2-Al_2O_3 glass (G69250; Heraeus, Germany) and 35 vol.% quartz as dispersion phase. In the following, this material will be referred to as "in35". The glass has a transformation temperature of 701°C. Above 850°C celsian ($BaAl_2Si_2O_8$) crystallizes from the glass. Its α of 9.4×10^{-6} K^{-1} (30–400°C)[23] is already close to the α of the thermoelectric materials. By varying the amount of dispersion phase according to Equation (1), the glass-ceramic composite should meet the following requirements: α of 11×10^{-6} K^{-1} (20–500°C), the sintering temperature of 900°C, and a high resistivity up to 800°C. This work focuses on the aspects of material development and compatibility. We present a co-sintered thermoelectric multilayer with respect to the reaction layers formed at the interfaces. A thorough evaluation of such a multilayer generator with respect to thermoelectric performance requires much additional

TABLE 1 Raw material properties used for calculation

	$\alpha_{20-400°C}$ (10^{-6} K^{-1})	E (MPa)	ν
SiO_2[21]	15	80	0.14
G69250*	8.4	81	0.22

*Values estimated by the model of Priven[24] (with software SciGlass 6.5) based on confidential glass composition of G69250.

information on design, measurement methods, and a review of comparable studies in the literature. Thus, such an evaluation is beyond the scope of the work presented here and will be presented in another dedicated report.

2 | EXPERIMENTAL PROCEDURE

2.1 | Calculation of compositions

Based on Equation (1) three different insulator compositions (in35, in45, and in55) from the mixture of SiO_2 (Sikron SF600; Quarzwerke Frechen, Germany) and BaO-B_2O_3-SiO_2-Al_2O_3-glass G69250 (Heraeus) were calculated using the material properties listed in Table 1. Starting from in35, three compositions were chosen to obtain averaged α in the range of the thermoelectric oxides (Table 2 and Figure 4).

2.2 | Sample preparation

Powder mixtures with varying amounts (Table 2) of SiO_2 (Sikron SF600; Quarzwerke Frechen) and glass G69250 (Heraeus) were attrition milled (moliNEx; Netzsch, Germany) for 1 h with ZrO_2 grinding media (d = 2–3 mm) in ethanol. After milling, the ethanol was evaporated using a rotary evaporator (Rotavapor R-124; Büchi). For dry pressing, pressing additives (1 wt% Optapix AC95 and 0.5 wt% Zusoplast 9002; both Zschimmer and Schwartz) were added to the powder mixture in an aqueous solution, which was then dried at 60°C and ground with an agate mortar. The so produced pressing granulates were uniaxially pressed to bars of 50 × 5 × 5 mm with 60 MPa (PW 10; Weber, Germany). The test bars were sintered at 900°C for 2 h. After sintering the specimens were cut in the desired dimensions. Additionally, in45 was additionally pressed to discs of d = 66 mm, height = 2 mm with 30 MPa (ES 247.02; Rucks, Germany).

To produce a screen-printable paste, 31 wt.% of a commercial screen-printing medium (801026; Ferro) was added to the powder mixture in45. The mixture was pre-homogenized with an agate mortar for 1 min and then homogenized for 1 h in a planetary ball mill (Pulverisette, Fritsch). 29 g of the mixture was ball milled in a 500 ml agate jar with 4 agate balls (Ø = 20 mm) with 300 min^{-1}. The paste was screen printed with a programmable screen-printer (P – 200A; Keko Equipment, Zuzemberk, Solvenia). The squeegee force was 60 N and the squeegee speed of the metal scraper (flood mode) was set to 75 mm/s and of the rubber squeegee to 50 mm/s, respectively. A 325 mesh screen (Koenen, Germany) was used. The paste was printed on $Ca_3Co_4O_9$ and $Ca_{0.98}Sm_{0.02}MnO_3$ ceramic green tapes. Detailed information is provided.[25]

The thermoelectric oxides were produced by the classical mixed oxide route. Stoichiometric amounts of $CaCO_3$ (99%, Riedel-de Häen), Co_3O_4 (99.97%, ChemPUR), $Sm(OH)_3$ (99.9%, Alfa-Ventron), and $MnCO_3$ (>99.9%, Aldrich Chemistry) were attrition milled (moliNEx; Netzsch) for 45 min with ZrO_2 grinding media (Ø = 2–3 mm) in ethanol to form the desired phase after calcination at 900°C for 12 h ($Ca_3Co_4O_9$) or 1250°C for 2 h ($Ca_{0.98}Sm_{0.02}MnO_3$). The calcined mixtures were then crushed with a planetary ball mill (agate grinding balls, 20 min, 215 min^{-1}; Pulverisette, Fritsch) and fine milled using an attrition mill (ZrO_2-grinding media, 800 s^{-1}, moliNEx; Netzsch) for 45 min ($Ca_3Co_4O_9$) or 4 h ($Ca_{0.98}Sm_{0.02}MnO_3$). The resulting mean grain size was 4 μm (laser diffraction method) for $Ca_3Co_4O_9$ and 0.1 μm (equivalent sphere diameter d_{VSSA} based on volume-specific surface area) for $Ca_{0.98}Sm_{0.02}MnO_3$. Tape casting slurries were produced by mixing the thermoelectric oxides with polyvenylbutyral (Eastman), dibutylphtalate (ACROS organics), rhodafac RE-610 (Solvay), and a solvent mixture containing ethanol (Merck), methylketon (Merck) and cyclohexanone (Merck) for 24 h in porcelain containers on a rolling bench. The slurries were tape cast on a tape casting machine (doctor blade method; Netzsch, Selb). The resulting tapes (width = 150 mm) had a thickness

TABLE 2 Physical properties of the insulators sintered at 900°C

	Powder: vol.% SiO_2	Powder: wt.% SiO_2	Sample: calculated α(20°C, 400°C) (10^{-6} K^{-1})	Sample: measured α(20°C, 400°C) (10^{-6} K^{-1})	Sample: apparent density (g/cm^3)	Sample: open porosity (%)	Sample: phase fraction (wt.%) celsian /glass/ quartz
in35	35	31	10.3	8.9	2.9	0.5 ± 0.0	21/51/29
in45	45	41	10.9	10.5	2.6	2.9 ± 0.8	13/51/36
in55	55	51	11.6	10.8	2.0	29.0 ± 0.1	11/42/48

of 150 μm ($Ca_3Co_4O_9$) or 85 μm ($Ca_{0.98}Sm_{0.02}MnO_3$). A commercial metallization paste AgPd (DP6146; Dupont) was screen-printed on top of the screen-printed insulation layer using the same screen-printing process, as explained before. The thermoelectric oxide green tapes with screen-printed insulation and metallization were stacked and laminated (custom-made heated stacking tool, 70°C, 20 MPa, 20 min). The multilayer laminates were sintered in a commercial low-temperature co-fired ceramics (LTCC)-sinter press (900°C, 7.5 MPa; ATV Technologie GmbH). Sintered mono-material stacks were used to determine the α_{ab} of the thermoelectric oxides.

2.3 | Characterization

The particle size distribution of the powders was analyzed using the laser diffraction method (Mastersizer 2000; Malvern Pananalytica) according to ISO 13320.[26] For powders finer than 0.7 μm, the equivalent sphere diameter d_{VSSA} was calculated with $d_{VSSA} = 6/S_M \times \rho_{true}$ from specific surface S_M and true density ρ_{true}.[27] Hereby, the specific surface was measured with the nitrogen adsorption method (NOVA 2200; Quantachrome) and the true density with He-gas pycnometry (AccuPyc II 1240; Micrometrics).

The linear shrinkage of the bar-shaped green samples was determined using a push-rod dilatometer with a heating rate of 10 K/min (DIL802; Bähr GmbH, Hüllhorst, Germany). The Archimedes method was used to determine the apparent density and open porosity of the sintered test bars.

The averaged α was measured with a push-rod dilatometer (DIL402c; Netzsch) on sintered test specimens with plane-parallel ends (length of 25 mm and width of 4 mm). The heating rate was set to 5 K/min and the contact force to 0.25 N. The averaged $\alpha(T_R, T)$ was calculated according to:

$$\alpha\left(T_{R,}\, T\right) \approx \left[l\left(T\right) - l_r\right] / \left[l_r\left(T - T_R\right)\right] \qquad (2)$$

with the length at room temperature (l_r), the temperature depending length $l(T)$, room temperature (T_R), and the measuring temperature (T). The measurement uncertainty is α(20°C, 200°C) = 0.64 × 10^{-6} K^{-1} and α(20°C, 500°C) = 0.37 × 10^{-6} K^{-1}, respectively.

The resistivity over temperature was measured using plane-parallel ground disc ($Ø$ = 50 mm) with fired Pt-electrodes (at 900°C, 6926; Heraeus) based on ASTM D 257 [28]. The measurement was performed in a tube furnace with a measurement cell (ProboStat; Norecs, Norway) and a high-resistance meter (4339B; Agilent) for recording. For the measurement at room temperature, the sample was mounted in a commercial resistivity cell (16008B; Agilent) The resistance was recorded until the measured value was constant. The measuring voltage was set between 1 V and 1000 V depending on the resistance. Each specimen was measured three times with at least 24 h of depolarization time. The resistivity was calculated according to Equation (3) with the resistance (R), the electrode area (A), and the thickness (h).

$$\rho_V = \left(R \cdot A\right) / h \qquad (3)$$

The paste homogeneity was analyzed by measuring the size of agglomerates with a grindometer (Model 232; Erichsen, Hemer, Germany). The screen-printed layer thicknesses were determined with the aid of a white light profilometer (μscan; NanoFocus AG, Oberhausen, Germany). Area and line scans were taken with a measuring frequency of 1000 Hz and a resolution in the x-direction of 5 μm. CLA 2.5 S/L was used as the sensor. The layer thickness was determined from the line scans using μsoft analysis V7 software (NanoFocus AG). An automatic linear shape correction was applied and the layer thickness was determined at 5 points each using the stepwise method.

The phase compositions were analyzed with powder X-ray diffraction (XRD, Ultima IV; Rigaku) with Cu-Kα-radiation (1.5418740 Å). Sintered test bars were crushed and then milled (Pulverisette 0, Fritsch with alumina inserts) to obtain powder finer than 63 μm. Diffractograms were analyzed with the Match!3 software package, using the Crystallography Open Database (COD) as a reference database. The quantitative phase fractions were determined using the Rietveld method (software: DIFFRAC.TOPAS 5; Bruker). Since the microstructure also contains a glass phase, a Partial or No Known Crystal Structure (PONKCS) phase was used to calculate the amorphous fraction. The PONKCS phase was created according to Scarlett and Madsen[29] using a mixture containing 91.5 wt.% glass G69250 and 8.5 wt.% ZnO.

The microstructure of the insulation materials and the multilayer samples was examined with scanning electron microscopy (SEM, Gemini Supra 40; Zeiss) on fractured and polished surfaces. To quantify the element concentrations of different phases, energy-dispersive X-ray spectroscopy (EDX, NSS 3.1; Thermofisher) was performed at U_A = 15 kV on at least five different spots in the sample. The corresponding spectra were evaluated using Pathfinder software (Version 1.3.22; Thermofisher). Estimates of the individual phase compositions were made from the results. The software package ImageJ was used to analyze the reaction layer thickness and the pore sizes of three micrographs. For each image, 15 data points were selected to determine the reaction layer thickness and 30 pores were measured to obtain the pore sizes, respectively.

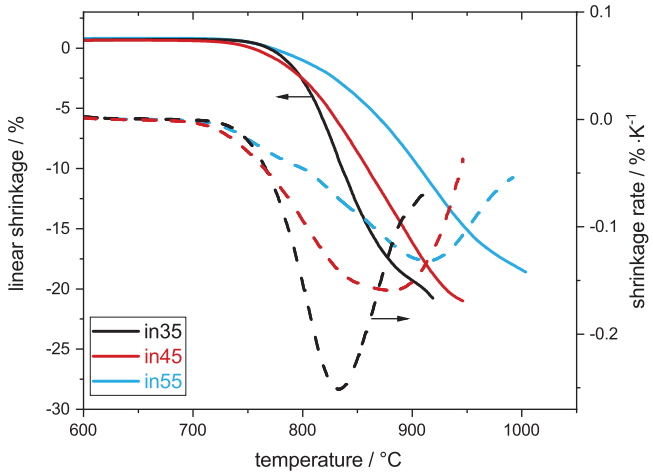

FIGURE 1 Shrinkage (left ordinate) and shrinkage rate (right ordinate) at a heating rate of 10 K/min

3 | RESULTS AND DISCUSSION

3.1 | Powder characteristics and shrinkage behavior

The powder mixtures in35, in 45, and in55 have very similar particle size distributions after attrition milling for 1 h with $d(0.1) = 0.9\,\mu$m, $d(0.5) = 2.3\,\mu$m, and $d(0.97) = 6.5\,\mu$m, respectively (laser diffraction method).

With decreasing glass and increasing quartz content, the shrinkage curves shift to higher temperatures (Figure 1). The temperature of the shrinkage rate maximum increases from 834°C for in35, to 882°C for in45, and to 914°C for in55. As known from the literature, the sintering mechanism of glass-ceramic composites is a non-reactive liquid phase sintering by the glass phase.[11] Therefore, the open porosity of the specimens that were sintered at 900°C increases (Table 2) with decreasing glass content.

3.2 | Phase composition and microstructure

Figure 2 shows the powder XRD patterns. The majority of reflections can be assigned to the phases quartz and celsian. Two minor reflections at 28.3° and 28.8° cannot be assigned to these two phases. This minor phase could be Ba_2SiO_4 (COD 96-154-2182). The intensity of this minor phase decreases with increasing SiO_2-content of the insulation material. In addition, the diffractograms show a glass hump. For the Rietveld analysis, the glass hump was quantified by the Partial or No Known Crystal Structures (PONCKS) phase. An exemplary Rietveld analysis is shown in Figure 2F for in55. The phase fractions (in wt.%) according to Rietveld analysis are summarized in Table 2. The quartz content after sintering is a few wt% lower than of the powder mixture. This could indicate a partial quartz solution in the glass phase. The celsian content and the glass content decrease with increasing SiO_2 content. The highest amount of celsian crystallizes in in35 (30 wt.% of the glass content), which leads to a significant decrease in glass content compared to the powder mixture. Higher amounts of quartz addition do not seem to be beneficial for celsian crystallization (only 20 wt.% from the glass crystallizes in in45 and in55).

As shown in Figure 3, the microstructure of the glass-ceramics is composed of a light matrix, elongated

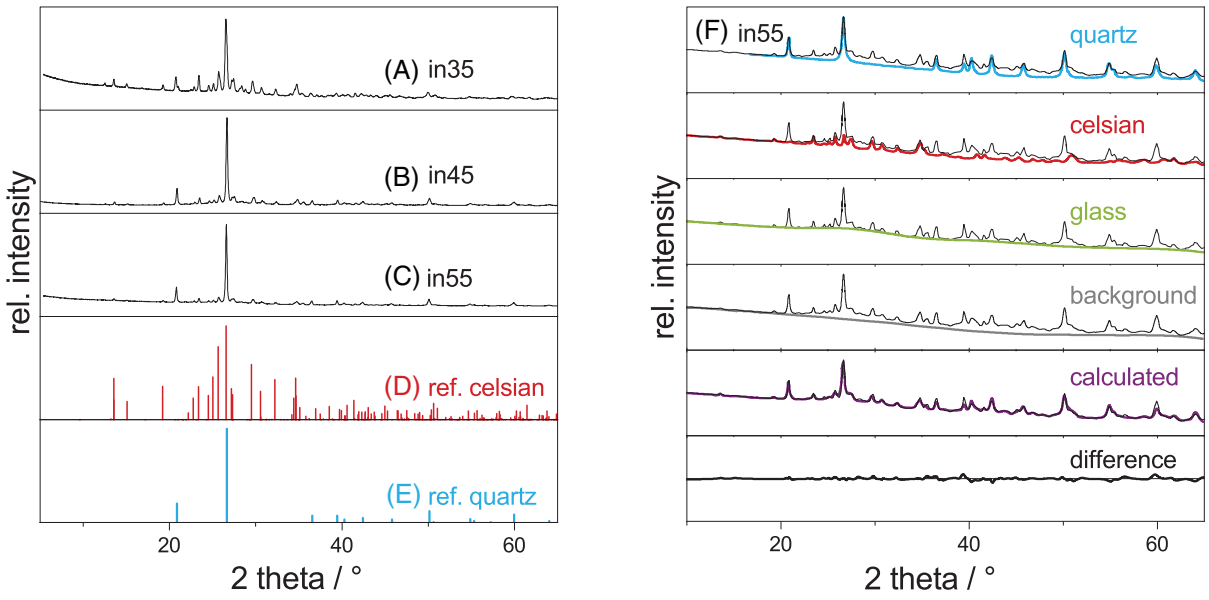

FIGURE 2 Powdered X-ray diffraction (XRD) of (A–C) sintered insulators and reference patterns of (D) celsian (COD: 96-900-0509), (E) quartz (COD: 96-900-5018), and (F) exemplary Rietveld analysis for in55

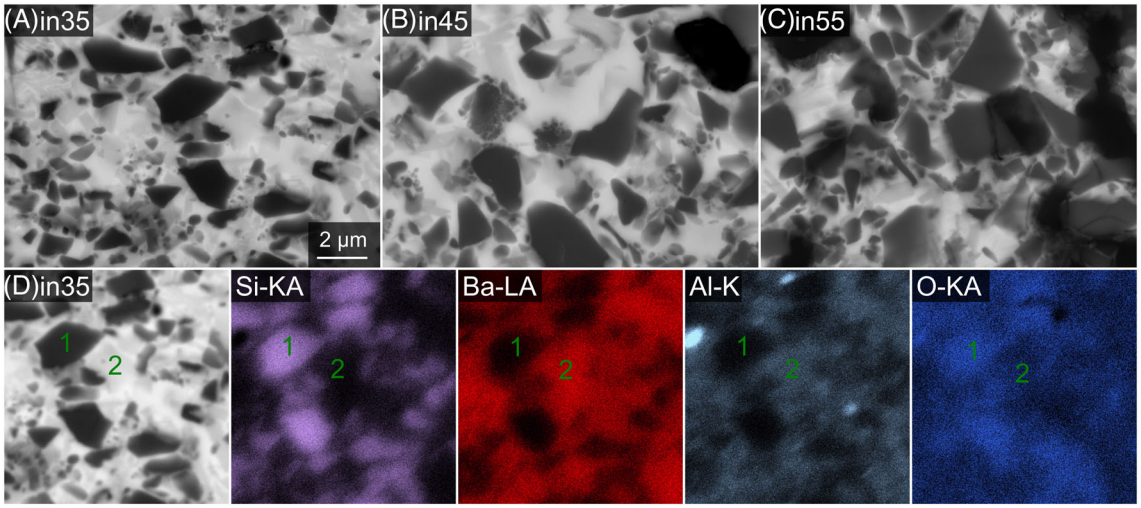

FIGURE 3 Scanning electron microscopy (SEM) images of polished samples (A-C) with back-scattered electron detector. (D) It shows the corresponding energy-dispersive X-ray spectroscopy (EDX)-Maps for in35, an exemplary dark crystallite marked with 1 and a light crystallite with 2

light crystallites, dark crystallites, and black pores. With increasing quartz content, the pore fraction increases and the amount of white crystallites decreases. The dark crystallites (see Figure 3D – indication 1) are Si (30 mol.%) and O (65 mol.%) rich and the light crystallites (indication 2) also contain Ba and Al. Together with the XRD results, the microstructure is therefore composed as follows: enclosed in a glass matrix are, on the one hand, the dispersion phase quartz (dark grains) and, on the other hand, the secondary phase celsian (light grains) that crystallizes during sintering.

3.3 | Thermal expansion

Figure 4 shows the averaged α of the thermoelectric materials and the insulators measured in ab-direction. Considering the material properties, only α of $Ca_3Co_4O_9$ is highly anisotropic. For the insulation materials, α should be isotropic. As shown in Figure 4, α_{ab} increases over temperature for all material systems shown here. For temperatures above 600°C, the α of the insulators are not shown in Figure 4. The glass phase reaches its glass transition region above 600°C, softens and thus α can no longer be determined. Additionally, a glass system above glass transition temperature can relax thermal stresses. Thus, it can be assumed that a not completely recrystallized glass-ceramic composite compensates for thermal mismatches of different layers as well.

The measured α increases with the increasing amount of SiO_2, confirming the prior calculation. The measured α for all compositions is lower than the calculated α. The differences amount from 0.4×10^{-6} K^{-1} for in45 to 1.4×10^{-6} K^{-1}

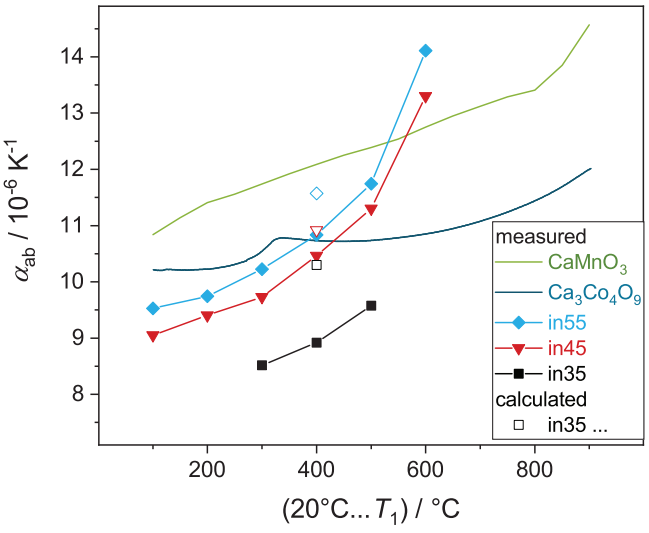

FIGURE 4 Averaged coefficient of thermal expansion α_{ab} in ab-direction. Calculated values are plotted as open symbols, whereas closed symbols indicate measured values

for in35. Celsian crystallization changes the composition of the insulation material. Since celsian has only a very low α of 2.5×10^{-6} K^{-1},[21] the calculated and measured values probably agree better with decreasing celsian content.

The different insulation materials vary in porosity. Following the mixing rule of Lundin[30] for composite materials, porosity does not affect the averaged α. Therefore, it is valid to compare the α of materials with different porosities.

Insulation material for co-fired thermoelectric generators based on $Ca_3Co_4O_9$ and $CaMnO_3$ should meet the following requirements: α should be in between the two

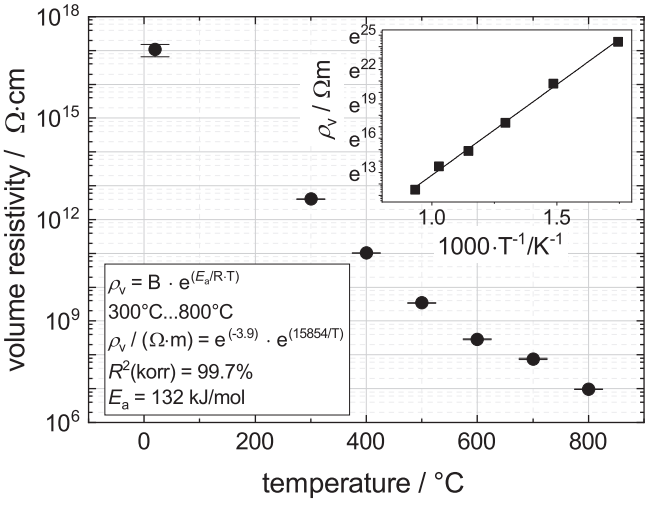

FIGURE 5 Volume resistivity of in45 over temperature with fitted regression. Arrhenius plot as an inserted diagram to calculate the activation energy

thermoelectric materials, the sintering temperature should be 900°C, and the porosity should be low. Since in45 is meeting these requirements best, it was thus chosen for resistivity measurements and screen-printing.

3.4 | Resistivity

As shown in Figure 5, the volume resistivity of in45 decreases over temperature, whereby all values exceed 10^6 Ωcm. Thus, the glass-ceramic composite is an electrical insulator in the whole temperature range with for insulators typical conductivity behavior over temperature. The high-temperature values (above 300°C) can be fitted with an Arrhenius function as proposed.[31] The activation energy (E_a) can be calculated from the slope of the Arrhenius plot and the gas constant (R). An E_a of 132 kJ mol^{-1} is in good accordance with literature data for glass systems [31]. In literature, a change in conductivity behavior is reported for glass at its transformation temperature [32]. The transformation temperature of G69250 is 701°C. For the glass-ceramic composite material in45, this change in conductivity behavior is not very pronounced as the high-temperature range can be well fitted with the same equation. Comparing the resistivity of in45 with literature data for glass-ceramic composite materials (low-temperature co-fired ceramics), in45 shows higher resistivity as 96% alumina and CT800 and is in the same range as DP951.[33] Please notice that the literature values were determined in AC and not DC-mode. At 800°C, the volume resistivity of in45 is more than eight magnitudes higher than the one of the thermoelectric oxides.[7,34] The insulator in45 should thus be suitable as an electrical insulation material for thermoelectric generators made from calcium cobaltite or calcium manganate.

3.5 | Screen-printed insulation and formed reaction layers

The fabricated screen-printing paste from in45 can be printed well. In single print mode, layer thicknesses of 22–24 μm after drying or 10 μm after sintering are achieved, respectively. The double print mode can increase the dry thickness to 28–34 μm. As shown in Figure 6B exemplarily for a unileg-generator, the screen-printed insulation shows a distinct corrugated profile in cross-section after sintering, which can be attributed to the screen mesh.

As shown in Figure 6, different reaction layers are formed in the multilayer during pressure-assisted co-sintering of insulation, thermoelectric oxides, and metallization. At the contact points between the AgPd metallization and in45, pores are formed in the in45 (see Figure 6C). The pores have diameters of up to 30 μm, but never completely rupture the insulation layer in the unileg-generator Please note that Figure 6C shows a representative micrograph regarding the average pore size. Pore formation in the contact zone between glass-ceramic and AgPd is known for LTCC.[35] Pd oxidizes in the air at 350°C to PdO and a reduction to Pd occurs at 800°C. Mixtures of Ag and Pd also show this oxidation and reduction behavior, but the stability range of PdO is smaller.[35] Moreover, oxidation is also described for the forming alloy of AgPd, which reaches its maximum of 20 mol.% Pd.[36] It can therefore be assumed that the pores within in45 are created by oxygen, which is released by the reduction of the AgPd mixture at around 800°C. In contrast to the thermoelectric oxides, the insulating layer is already so densely sintered at the temperature at which the reduction of PdO to Pd takes place that the gas phase can no longer escape. Pores are formed, which expand in the further heating process. The formation of pores could be prevented by two different measures: the use of Ag instead of AgPd as metallization, or the use of in55 instead of in45. The in55 sinters at higher temperatures and is therefore not dense in the temperature of the gas release. However, in55 could lead to short circuits due to its high open porosity of 29%.

Various reaction layers are formed in the contact zone between thermoelectric oxides and insulation. In Figure 6D–F, these layers are denoted with numbers. Their elemental compositions were analyzed with EDX at three points for each layer. Phases were assumed based on the results. Please note, that these phases are only assumptions as the elemental analysis with EDX is not very accurate. The compositions of the reaction layers are summarized in Table 3. Two different reaction layers are found

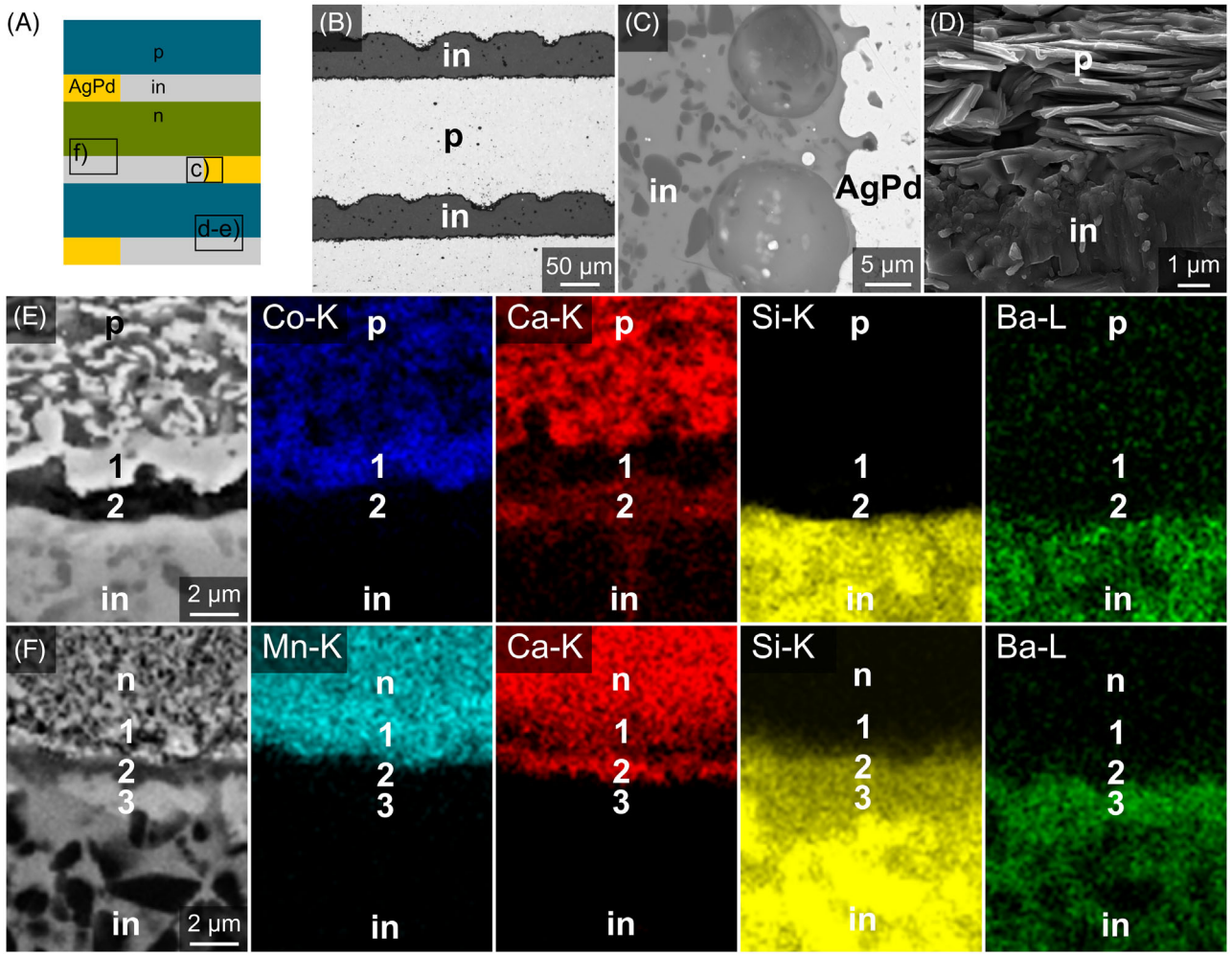

FIGURE 6 Representative Scanning electron microscopy (SEM) images (SE-detector) of screen printed insulation in45 after sintering with SE-detector. (A) Schematic drawing of a multilayer generator with the analyzed contact zones, (B) $Ca_3Co_4O_9$ (p) – insulation (in) – multilayer, (C) contact zone of in45 with metallization (AgPd–DP6145), (D) fracture surface of the reaction zone between $Ca_3Co_4O_9$ and in45 (InLense detector), (E) reaction zone between $Ca_3Co_4O_9$ and in45 with associated energy-dispersive X-ray spectroscopy (EDX) distribution maps, and (F) reaction zone between $CaMnO_3$ (n) and in45 with associated EDX distribution maps

TABLE 3 Energy-dispersive X-ray spectroscopy (EDX)-analysis of formed reaction layers and assumed phases

Reaction layers in between of	No.	Elements (mol.%)	Assumed phases	Layer thickness (μm)
c) in45 + AgPd		–	Pores	3–30
e) in45 + $Ca_3Co_4O_9$	1	Co–O 55–44	Co_3O_4	2
	2	Ca–O 33–67	CaO	1
f) in45 + $CaMnO_3$	1	Ca–Mn–O 12–25–63	$CaMn_2O_4$	2
	2	Ca–Si –O 16–22–62	$CaSiO_3$	1
	3	Ba–Ca–Si–O 6–5–30–59	Barium silicate, Ca-containing	Crystallites

between $Ca_3Co_4O_9$ and in45 (see Figure 6E). A Co-rich layer of 1–2 μm forms in the contact zone with $Ca_3Co_4O_9$, which is probably Co_3O_4. This layer is followed by a porous Ca-rich layer. The porosity is probably an artifact of the polishing as the fracture surface does not show any pores (see Figure 6D). It is assumed that the Ca-rich phase is CaO, which is known to form $Ca(OH)_2$ in contact with water (as used during polishing). Due to its high reactivity with water, a CaO reaction layer could be critical for future applications. Wolf et al. reported the formation of a similar 2 μm reaction layer of CaO and Co_3O_4 in the contact zone of $Ca_3Co_4O_9$ and a commercial LTCC (DP951).[37] DP951 is a glass-ceramic composite material based on an alumo-silicate glass and contains more Al_2O_3 and less SiO_2 than in45. As two glass-ceramics with very different compositions lead to the formation of similar reaction layers, it can be assumed that the formation of these reaction layers cannot be prevented, for example, by composition variations.

Three reaction layers form between $CaMnO_3$ and in45 (see Figure 6F). $CaMnO_3$ is followed by an Mn-rich layer of 2 μm, which could be $CaMn_2O_4$. The second layer with a thickness of 1 μm is Ca-rich and Si-rich and may be assigned to $CaSiO_3$. In the insulation layer, crystallites that appear white in the SEM images with a diameter of 2 to 4 μm are formed at the contact area. These crystallites do not form a continuous layer and they are Ba-rich. Based on the composition obtained by EDX, it could be a calcium-containing barium silicate.

The thicknesses of the reaction layers are very small and in45 is, therefore, suitable for co-sintering with $CaMnO_3$ and $Ca_3Co_4O_9$.

4 | SUMMARY

In this study, an insulation layer for thermoelectric multilayer generators from calcium cobaltite and calcium manganate was developed. The insulation material should thereby meet the following requirements: an averaged α in between of the thermoelectric oxides (11×10^{-6} K^{-1} from 20–500°C), a sintering temperature of 900°C, a high resistivity up to 800°C, and a good co-sinterability. Glass-ceramic composites are especially suited as insulators as their physical properties can be tuned by varying glass and dispersion phases. Based on a glass-ceramic composite from literature,[21,23] three different compositions consisting of a BaO-B_2O_3-SiO_2-Al_2O_3-glass and varying quartz-content as dispersion phase were fabricated. Prior to that, α of these compositions was calculated using the equation of Nazare and Ondracek.[22]

After sintering at 900°C, the insulation materials contain quartz grains, celsian, and a residual glass phase. With increasing SiO_2-content, celsian crystallization from the glass phase decreases, the open porosity increases, and α increases. This study showed that the calculated and the measured α agree well. The composition in45, with 45 vol.% of quartz phase, meets the requirements the best. The in45 shows a high resistivity over temperature and was successfully processed further to a screen-printable paste. Multilayer samples of calcium cobaltite, calcium manganate, and in45 show minor reaction layers, which should not hinder an eventual application.

ACKNOWLEDGMENTS

The authors want to thank all BAM colleagues for contributing to this study. Special gratitude to A. Gardei for XRD measurements, S. Benemann and R. Saliwan Neumann for SEM micrographs, C. Meyer for determination of α, J. Biberstein for dilatometry and resistivity measurements, F. Lindemann for determining the density and porosity, and B. Schulz for assisting in screen-printing. For providing several screen-printing media, we want to thank S. Schäfer from Ferro GmbH, Frankfurt, Germany.

Open access funding enabled and organized by Projekt DEAL.

CONFLICT OF INTEREST

The authors declare that they have no conflict of interest.

ORCID

Sophie Bresch https://orcid.org/0000-0003-2490-7208
Björn Mieller https://orcid.org/0000-0002-0784-9790
Ralf Moos https://orcid.org/0000-0001-7622-0120

REFERENCES

1. Hayashi SF, Nakamura T, Kageyama K, Takagi H. Monolithic thermoelectric devices prepared with multilayer cofired ceramics technology. Jpn J Appl Phys. 2010;49(9):096505.
2. Funahashi S, Nakamura T, Kageyama K, Ieki H. Monolithic oxide–metal composite thermoelectric generators for energy harvesting. J Appl Phys. 2011;109(12):124509.
3. Teichert S, Bochmann A, Reimann T, Schulz T, Dreßler C, Udich S, et al. A monolithic oxide-based transversal thermoelectric energy harvester. J Electron Mater. 2016;45(3):1966–9.
4. Töpfer J, Reimann T, Schulz T, Bochmann A, Capraro B, Barth S, et al. Oxide multilayer thermoelectric generators. Int J Appl Ceram Tec. 2017;15(3):716–22.
5. Fergus JW. Oxide materials for high temperature thermoelectric energy conversion. J Eur Ceram Soc. 2012;32(3):525–40.
6. Koumoto K, Funahashi R, Guilmeau E, Miyazaki Y, Weidenkaff A, Wang Y, et al. Thermoelectric ceramics for energy harvesting. J Am Ceram Soc. 2013;96(1):1–23.
7. Bresch S, Mieller B, Schönauer-Kamin D, Moos R, Reimann T, Giovannelli F, et al. Influence of pressure and dwell time on pressure-assisted sintering of calcium cobaltite. J Am Ceram Soc. 2021;104(2):917–27.
8. Reimann T, Bochmann A, Vogel A, Capraro B, Teichert S, Töpfer J. Fabrication of a transversal multilayer thermoelectric

generator with substituted calcium manganite. J Am Ceram Soc. 2017;100(12):5700–8.
9. Barsoum MW. Fundamentals of ceramics. 1st ed, Bristol: Institute of Physics Publishing; 2003.
10. Varshneya AK. Fundamentals of inorganic glasses. 1st ed, London: Academic Press; 1993.
11. Rabe T, Schiller WA, Hochheimer T, Modes C, Kipka A. Zero shrinkage of LTCC by self-constrained sintering. Int J Appl Ceram Tec. 2005;2(5):374–82.
12. Urata S, Funahashi R, Mihara T, Kosuga A, Sodeoka S, Tanaka T. Power Generation of a p-Type $Ca_3Co_4O_9$/n-Type $CaMnO_3$ Module. Int J Appl Ceram Tec. 2007;4(6):535–40.
13. Leonidova EI, Leonidov IA, Patrakeev MV, Kozhevnikov VL. Oxygen non-stoichiometry, high-temperature properties, and phase diagram of $CaMnO_{3-\delta}$. J Solid State Electrochem. 2011;15(5):1071–5.
14. Yu S, He S, Chen H, Guo L. Effect of calcination temperature on oxidation state of cobalt in calcium cobaltite and relevant performance as intermediate-temperature solid oxide fuel cell cathodes. J Power Sources. 2015;280:581–7.
15. Kenfaui D, Chateigner D, Gomina M, Noudem JG. Anisotropy of the mechanical and thermoelectric properties of hot-pressed single-layer and multilayer thick $Ca_3Co_4O_9$ ceramics. Int J Appl Ceram Tec. 2011;8(1):214–26.
16. Kanas N, Bittner M, Desissa TD, Singh SP, Norby T, Feldhoff A, et al. All-oxide thermoelectric module with in situ formed non-rectifying complex p–p–n junction and transverse thermoelectric effect. ACS Omega. 2018;3(8):9899-906.
17. Kolobekken SH. All oxide thermoelectric device based on Ca0.931Mn0.98Ta0.02O3-δ-Ca3Co4O9 pn-junction [Master thesis]: Norwegian University of Science and Technology; 2017. Available from: http://hdl.handle.net/11250/2453061.
18. Hsu C-S, Huang C-L. Effect of CuO additive on sintering and microwave dielectric behavior of $LaAlO_3$ ceramics. Mater Res Bull. 2001;36(11):1939–47.
19. Gupta TK. Sintering of MgO: densification and grain growth. J Mater Sci. 1971;6(1):25–32.
20. Popescu B, Enache S, Ghica C, Valeanu M. Solid-state synthesis and spark plasma sintering of $SrZrO_3$ ceramics. J Alloys Compd. 2011;509(22):6395–9.
21. Eberstein M, Glitzky C, Gemeinert M, Rabe T, Schiller WA, Modes C. Design of LTCC with high thermal expansion. Int J Appl Ceram Tec. 2009;6(1):1–8.
22. Nazare S, Ondracek G. Zum Zusammenhang zwischen Eigenschaften und Gefügestruktur mehrphasiger Werkstoffe. Teil IV: Gefügestruktur und thermischer Ausdehnungskoeffizient. Materialwiss Werkstofftech. 1978;9(4):140–7.
23. Brandt B, Gemeinert M, Rabe T, Bolte J. Low-temperature co-fired ceramic substrates for high-performance strain gauges. Int J Appl Ceram Tec. 2013;10(3):413–20.
24. Priven AI. General method for calculating the properties of oxide glasses and glass forming melts from their composition and temperature. Glass Technol. 2004;45(6):244–54.
25. Bresch S, Mieller B, Schoenauer-Kamin D, Moos R, Giovanelli F, Rabe T. Influence of pressure assisted sintering and reaction sintering on microstructure and thermoelectric properties of bi-doped and undoped calcium cobaltite. J Appl Phys. 2019;126(7):075102.
26. ISO 13320:2020. Particle size analysis – laser diffraction. 2nd ed. Berlin: ISO; 2020.
27. Wohlleben W, Mielke J, Bianchin A, Ghanem A, Freiberger H, Rauscher H, et al. Reliable nanomaterial classification of powders using the volume-specific surface area method. J Nanopart Res. 2017;19(2):61.
28. ASTM D257-14. Standard test methods for DC resistance or conductance of insulating materials. Conshohocken, PA: ASTM International; 2014.
29. Scarlett NVY, Madsen IC. Quantification of phases with partial or no known crystal structures. Powder Diffr. 2006;21(4):278–84.
30. Lundin ST. Studies on triaxial whiteware bodies. Stockholm: Almquist & Wiksell; 1959.
31. Kingery WD, Bowen HK, Uhlmann DR. Introduction to ceramics. 2nd ed. New York: Wiley; 1976.
32. Startsev YK. Technique for measuring the electric conductivity of glasses and melts over a wide temperature range covering the glass transition region. Glass Phys Chem. 2000;26(2):73–82.
33. Kita J, Engelbrecht A, Schubert F, Groß A, Rettig F, Moos R. Some practical points to consider with respect to thermal conductivity and electrical resistivity of ceramic substrates for high-temperature gas sensors. Sens Actuators, B. 2015;213:541–6.
34. Bresch S, Mieller B, Delorme F, Chen C, Bektas M, Moos R, et al. Influence of reaction-sintering and calcination conditions on thermoelectric properties of sm-doped calcium manganate $CaMnO_3$. J Ceram Sci Technol. 2018;9(3):289–99.
35. Wang SF, Dougherty JP, Huebner W, Pepin JG. Silver-palladium thick-film conductors. J Am Ceram Soc. 1994;77(12):3051–72.
36. Garino T, Rodriguez M. Behavior of silver and palladium mixtures during heating. J Am Ceram Soc. 2000;83(11):2709–14.
37. Wolf M, Abt M, Hoffmann G, Overmeyer L, Feldhoff A. Ceramic-based thermoelectric generator processed via spray-coating and laser structuring. Open Ceram. 2020:1;100002.

How to cite this article: Bresch S, Mieller B, Mrkwitschka P, Moos R, Rabe T. Glass-ceramic composites as insulation material for thermoelectric oxide multilayer generators. J Am Ceram Soc. 2021;1–10.
https://doi.org/10.1111/jace.18235